Biomaterials 276 (2021) 120996

Contents lists available at ScienceDirect

Biomaterials

journal homepage: www.elsevier.com/locate/biomaterials

An artificial membrane binding protein-polymer surfactant nanocomplex facilitates stem cell adhesion to the cartilage extracellular matrix

Rosalia Cuahtecontzi Delint [a,b], Graham J. Day [a], William J.P. Macalester [a,b], Wael Kafienah [a], Wenjin Xiao [a,**], Adam W. Perriman [a,c,*]

[a] School of Cellular and Molecular Medicine, University of Bristol, BS8 1TD, UK
[b] Bristol Centre for Functional Nanomaterials, University of Bristol, BS8 1FD, UK
[c] BrisSynBio Synthetic Biology Research Centre, University of Bristol, BS8 1TQ, UK

ARTICLE INFO

Keywords:
Articular cartilage repair
Stem cell therapy
Cell membrane re-engineering
Protein-polymer surfactant complex
Cell adhesion

ABSTRACT

One of the major challenges within the emerging field of injectable stem cell therapies for articular cartilage (AC) repair is the retention of sufficient viable cell numbers at the site of injury. Even when delivered *via* intra-articular injection, the number of stem cells retained at the target is often low and declines rapidly over time. To address this challenge, an artificial plasma membrane binding nanocomplex was rationally designed to provide human mesenchymal stem cells (hMSCs) with increased adhesion to articular cartilage tissue. The nanocomplex comprises the extracellular matrix (ECM) binding peptide of a placenta growth factor-2 (PlGF-2) fused to a supercharged green fluorescent protein (scGFP), which was electrostatically conjugated to anionic polymer surfactant chains to yield [S$^-$]scGFP_PlGF2. The [S$^-$]scGFP_PlGF2 nanocomplex spontaneously inserts into the plasma membrane of hMSCs, is not cytotoxic, and does not inhibit differentiation. The nanocomplex-modified hMSCs showed a significant increase in affinity for immobilised collagen II, a key ECM protein of cartilage, in both static and dynamic cell adhesion assays. Moreover, the cells adhered strongly to bovine *ex vivo* articular cartilage explants resulting in high cell numbers. These findings suggest that the re-engineering of hMSC membranes with [S$^-$]scGFP_PlGF2 could improve the efficacy of injectable stem cell-based therapies for the treatment of damaged articular cartilage.

1. Introduction

Articular cartilage (AC) damage arising from trauma or osteoarthritis is extremely common, and is a major cause of pain and disability in aging populations [1]. Due to the limited self-renewal capacity of cartilage, surgical intervention has remained the leading treatment to help alleviate pain and improve joint mobility. Unfortunately, surgical approaches, such as bone marrow stimulation and osteochondral autograft transplantation, are limited by tissue availability, immunological responses, and the high demands of invasive surgeries, resulting in only short-term effectiveness on small defects [2]. Accordingly, there is an unmet clinical need for new treatment strategies for AC damage.

Injectable stem cell therapies are in pre-clinical development for a range of indications [2–4] and are emerging as next generation candidates for AC damage [5]. Intra-articular (IA) injection of stem cells is clinically facile and relatively non-invasive, making it a potentially efficient treatment for cartilage repair. Several clinical trials have now concluded that the implantation of stem cells successfully improves knee joint mobility and results in the formation of new hyaline-like cartilage [6–8].

Mesenchymal stem cells (MSCs) have a number of desirable attributes that are key for the development of autologous cell therapies for AC repair. They are readily available and can be expanded rapidly, exhibit immunomodulatory [9,10] and anti-inflammatory properties [11] through secretion of trophic factors that regulate paracrine signalling [12,13] or extracellular vesicles containing active signalling molecules [14,15], and can differentiate into chondrocytes [16]. Significantly, a recent study using an immunocompetent transgenic rodent model showed that IA injections of murine MSCs engrafted to regenerate cartilage in full-thickness defects *via* a nonprogenitor-mediated mechanism [17].

The exact mechanisms underlying how MSCs contribute to cartilage

* Corresponding author. School of Cellular and Molecular Medicine, University of Bristol, BS8 1TD, UK.
** Corresponding author. School of Cellular and Molecular Medicine, University of Bristol, BS8 1TD, UK.
E-mail address: chawp@bristol.ac.uk (A.W. Perriman).

https://doi.org/10.1016/j.biomaterials.2021.120996
Received 8 December 2020; Received in revised form 12 May 2021; Accepted 24 June 2021
Available online 28 June 2021

repair have not yet been clearly elucidated. Chondrogenic differentiation, immunomodulation, and the production of paracrine signalling mostly likely play a key role [18]. Notably, MSCs have been shown to engraft and produce new tissue when cells remained in the damaged area of cartilage [19,20]. Accordingly, it is becoming apparent that transplanted MSCs need to remain at the site of injury in order to achieve a significant therapeutic effect. Indeed, a lack of targeting presents a potential barrier to the widespread clinical translation of injectable MCS-based therapies for AC repair, where off-target effects result in low engraftment, even in low flow environments such as the joint capsule [21]. For example, in a rabbit model, MSCs that were intra-articularly injected into the injured knee were found to migrate to the suprapatellar bursa (upper knee), to the popliteal fossa (back of the knee joint), and to the subchondral femur bone, resulting in low efficacy for cartilage repair [22].

Such low levels of cell retention in the AC can be rationalised by poor cell adhesion at the site of injury post injection, which is mediated by AC surface bound anti-adhesive molecules such as lubricin [23]. Ideally, after articular implantation, MSCs would migrate to the damaged site by following chemoattractant signals released by the disruption of the extracellular matrix (ECM). After initial contact, MSCs would roll and arrest *via* adhesion molecule-receptor interactions, followed by cytoskeletal rearrangement and engraftment to the ECM [24,25]. Failure to accomplish cell–ECM interactions can result in *anoikis* (cell homelessness) and apoptosis [21]. Therefore, building appropriate interactions between MSCs and the ECM is crucial to promote cell viability, retention, engraftment, and repair.

Several tissue engineering approaches been developed in order to improve stem cell retention, mainly by utilizing soft scaffolding materials. For instance, cells have been implanted using soft biocompatible matrices such as collagen [26] or alginate [27] hydrogels [28]. Although these substrates provide additional support for cell survival, retention and wound healing, major hurdles still remain, such as cartilage biomechanical compatibility and foreign body reactions [29]. Indeed, despite biodegradability and extrudability being attractive properties of hydrogel-based scaffolds, they are susceptible to mechanical failure, as most hydrogels undergo bulk erosion [30]. Moreover, when hydrogels are used for AC regeneration, there is a trade-off between stiffness to support the mechanical loads and degradability due to compression [31].

Cell membrane re-engineering is emerging as a new approach to improve the targeting performance of therapeutic stem cells in regenerative medicine. For instance, Cheng et al. re-engineered the membrane of MSCs using surface chemistry to covalently conjugate E-selectin binding peptides in order to modulate cell rolling and adhesion [32]. Another notable example was by Lo et al., who used non-covalent interactions to decorate MSCs with the human antibody (IgG1) fused to P-selectin glycoprotein ligand-1 [33]. These modified cells showed superior rolling and adhesion capacities for P-selectin- and E-selectin--modified surfaces, leading to enhanced MSC tethering to human umbilical vein endothelial cells (HUVECs). Similarly, a recent study by Wu et al. demonstrated that MSCs were directed to and retained at infarcted heart tissue after membrane biotinylation and conjugation to a streptavidin-intermediated antibody specific to intercellular cell adhesion molecules [34]. Nevertheless, to our knowledge, a MSC membrane re-engineering strategy for improved articular cartilage adhesion has not been reported.

Previously, our group described a new cell membrane re-engineering methodology, where exogenous protein molecules could be directly displayed on the plasma membrane of stem cells to provide additional functionality. This was achieved by utilizing genetically or chemically supercharged proteins that are electrostatically conjugated to anionic polymer surfactant molecules with high membrane binding affinities. We have demonstrated that several functional proteins can be readily displayed on the surface of human MSCs (hMSCs) to improve their performance both *in vitro* and *in vivo*. These include, the oxygen-binding protein myoglobin, which improved the quality and distribution of *in vitro* engineered cartilage tissue [35], an artificial membrane binding thrombin, which facilitated hMSC membrane nucleated fibrin-hydrogel scaffold formation [36], and a bacterial adhesion protein chimera that directed stem cells to the myocardium [37]. In all cases, conjugation of the supercationic protein with the polymer-surfactant increased the persistence time of the nanocomplexes at the plasma membrane of the hMSCs.

Here, the conceptual advance is centred on improving cell adhesion to AC by displaying an ECM-binding peptide motif from placenta growth factor 2 ($PlGF2_{123–14}$; PlGF2 to simplify) [38] on the membrane of hMSCs. To do this, the PlGF2 peptide sequence was incorporated into an artificial membrane-binding construct by fusion with a supercharged green fluorescent protein (scGFP+36; scGFP for simplicity) [39], which was electrostatically conjugated to oxidised polyoxyethylene nonylphenyl ether (S^-) to yield [S^-]scGFP_PIGF2 (Fig. 1). A broad range of biophysical techniques were used to study the structure of the novel fusion protein and resulting nanocomplex, which showed that the protein structure and functions were preserved and that the PIGF2 peptide motif was accessible not obstructed by the scGFP domain. When introduced to hMSCs, the [S^-]scGFP_PIGF2 spontaneously inserted into the plasma membrane without cytotoxicity and showed no suppression of cell proliferation or differentiation. Notably, hMSCs showed significantly increased adhesion to collagen II after modification, under both static and dynamic conditions. Moreover, hMSCs modified with [S^-] scGFP_PIGF2 showed improved cell adhesion performance on the articular surface of live bovine cartilage explants.

2. Results and discussion

2.1. Expression and characterisation of the recombinant fusion protein scGFP_PIGF2

The fusion protein scGFP_PlGF2 (Supplementary Table 1) and the control protein scGFP were expressed in *E. coli*, isolated *via* immobilised metal-ion affinity chromatography, and analysed by SDS–PAGE to assess purity. Single bands were observed at approximately 32 kDa and 29 kDa for scGFP_PlGF2 and scGFP, respectively, and matrix-assisted laser desorption/ionisation mass spectrometry (MALDI-MS) gave respective molecular weights of 32.110 kDa and 29.275 kDa (Supplementary Figure 1 and 2). The difference in m/z ratios between the proteins corresponded well with the predicted molecular weight of the PlGF2 peptide (Supplementary Table 2). Given that scGFP_PlGF2 fusion was rationally designed to display the PlGF2 peptide when cell membrane bound, protein structure modelling was performed *via* iterative threading assembly simulations (I-TASSER) to determine the orientation of the peptide with respect to the globular scGFP domain [40] (see Experimental section 4.8). Although no crystal structure is available for scGFP, these models predicted that the scGFP domain folded into a β-barrel similarly to superfolder GFP (the template protein structure for scGFP) with the PIGF2 domain extended out away from the C-terminus of the scGFP (Supplementary Fig. 3a and b) [39,41]. Consequently, experimental studies comparing scGFP_PlGF2 to scGFP were undertaken to evaluate the folding of the scGFP domain and confirm the steric accessibility of the PlGF2 peptide.

Deconvolution of near-UV synchrotron radiation–circular dichroism (SR–CD) spectra (Fig. 2a and Supplementary Table 3) revealed comparable secondary structure proportions between scGFP and scGFP_PlGF2, and UV–vis and fluorescence spectroscopy studies confirmed their near identical optical properties (Supplementary Figure 4 and 5), verifying the correct folding and fluorophore maturation of the scGFP domain in scGFP_PlGF2. Dynamic light scattering (DLS) measurements revealed that the addition of the PlGF2 peptide sequence to scGFP increased the hydrodynamic diameter from 4.6 ± 0.3 nm to 5.6 ± 0.7 nm (Fig. 2b). Synchrotron radiation–small angle X-ray scattering (SR–SAXS) highlighted structural differences between scGFP_PlGF2 and scGFP at higher

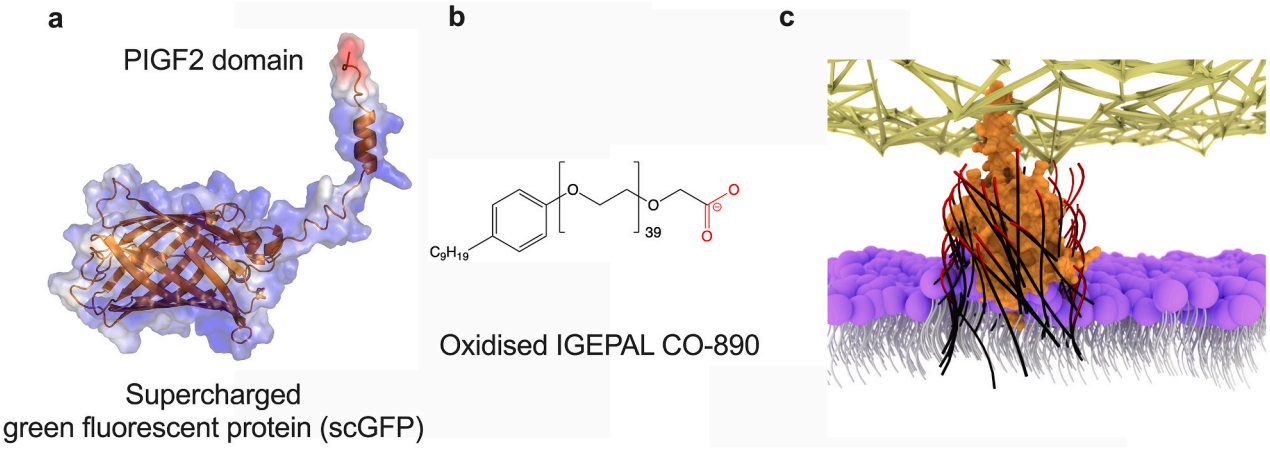

Fig. 1. Schematic representation of the nanocomplex. **a** Three-dimensional ribbon model of scGFP_PIGF2 (orange) enveloped within a surface model signifying the electrostatic potential of the protein (blue: positive; red: negative). **b** The anionic polymer surfactant that was electrostatically conjugated to the surface of scGFP_PIGF2. **c** Graphical representation of the nanocomplex [S$^-$]scGFP_PIGF2 (anionic polymer surfactant is blue and the protein is orange) embedded within a cell membrane (magenta spheres with white tails) and bound to extracellular matrix (yellow web). (For interpretation of the references to colour in this figure legend, the reader is referred to the Web version of this article.)

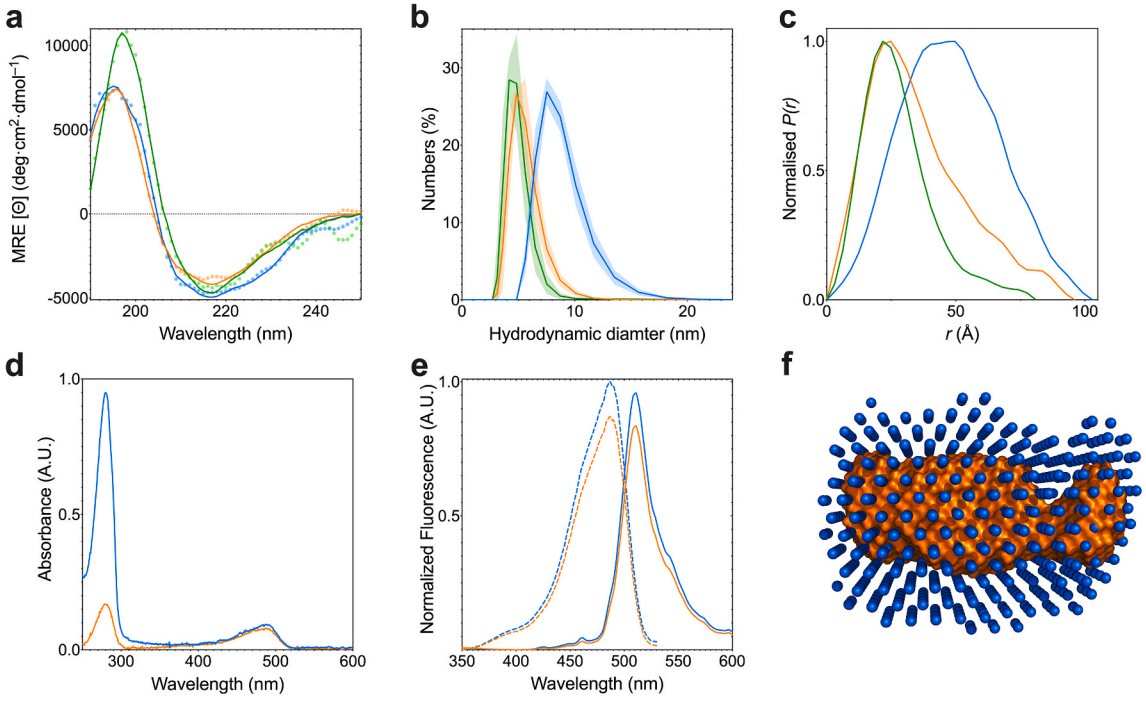

Fig. 2. Structural and biophysical characterisation of the nanoconstructs. **a** Synchrotron radiation–circular dichroism spectra from scGFP (green circles), scGFP_PlGF2 (orange circles) and [S$^-$]scGFP_PlGF2 (blue circles) with corresponding fits (solid lines). Data was fitted with BestSel and normalised root-mean-squared deviation values for scGFP, scGFP_PlGF2 and [S$^-$]scGFP_PlGF2 are 0.1436, 0.0570, and 0.0852, respectively. Measurements were taken at 36 °C at a concentration of 0.35 mg mL^{-1}. **b** Hydrodynamic diameter numbers distribution obtained by dynamic light scattering for scGFP, scGFP_PlGF2, and [S$^-$]scGFP_PlGF2. Solid lines present averages with standard error displayed as coloured areas, n = 3. Measurements were taken in 400 mM NaCl and 20 mM Tris-HCl buffer at pH 7.5. **c** The radial probability distribution function (*P(r)*) of the scGFP, scGFP_PlGF2, and [S$^-$]scGFP_PlGF2. **d** UV–vis spectroscopy of scGFP_PlGF2 and [S$^-$]scGFP_PlGF2. Measurements were taken in buffer 400 mM sodium chloride, 20 mM Tris-HCl in pH 7.5. **e** Fluorescence spectroscopy of scGFP_PlGF2 and [S$^-$]scGFP_PlGF2, displaying excitation (dashed lines) and emission (solid lines) data. Measurements were taken in buffer 400 mM NaCl and 20 mM Tris-HCl at pH 7.5. **f** *Ab initio* bead model calculated from synchrotron radiation–small angle scattering (SR–SAXS) data, displaying the scGFP_PIGF2 (orange surface) within the [S$^-$]scGFP_PlGF2 (blue spheres) model. (For interpretation of the references to colour in this figure legend, the reader is referred to the Web version of this article.)

resolution.

Resolution (Supplementary Figure 6 and Supplementary Table 4). The presence of the PlGF2 peptide resulted in a 7 Å increase to the radius of gyration (R_g) and a 15 Å increase in the maximum dimension of the pair distribution function (D_{max}; Fig. 2c and Supplementary Table 4), which supported the DLS data. The Porod exponent (P_E) for scGFP_PlGF2, a measure of molecule flexibility, decreased when compared to scGFP, signifying greater structural flexibility (Supplementary Table 4) [42]. *Ab initio* models were constructed using the SR–SAXS data to further investigate the conformation and hence the steric accessibility of the PlGF2 peptide (see Experimental section 4.8). The resulting scGFP_PlGF2 models exhibited high-aspect ratios with a

wide tail region corresponding to the PIGF2 peptide extending away from the scGFP moiety (Supplementary Figure 3c). Taken together, these data indicated that the scGFP domain was correctly folded and that the PlGF2 peptide was likely sterically accessible for ECM binding.

2.2. Formation and structure of the nanocomplex [S⁻]scGFP_PlGF2

In light of the retention of structure and function by scGFP_PlGF2, the anionic polymer surfactant, S^- ($H_{19}C_9$-Ph–$(CH_2CH_2O)_{39}$–O–CH–COO^-), was used to generate an electrostatically-stabilised polymer surfactant corona on the surface of the supercharged fusion protein [35,37,43,44] (Fig. 1). UV–vis spectroscopy from the [S⁻]scGFP_PlGF2 nanohybrid dispersion revealed a protein positive charge:surfactant stoichiometric ratio of at 1.4:1 (Fig. 2d), which indicated a small excess of protein-bound surfactant chains. Deconvolution of the SR–CD spectra from [S⁻]scGFP_PlGF2 showed a high proportion of β-sheet secondary structure, with similar levels to that found in scGFP and scGFP_PlGF2 (Fig. 2b and Supplementary Table 3) [41]. The preservation of the protein tertiary structure was supported by fluorescence spectroscopy measurements, which illustrated the retention of scGFP fluorophore geometry, with a maximum absorbance at 487 nm and excitation at 511 nm (Fig. 2e) [39,41].

Zeta potentiometry showed a reduction in the zeta potential upon electrostatic assembly, decreasing from $+21 \pm 0.8$ mV for scGFP_PlGF2 to -0.5 ± 0.5 mV for [S⁻]scGFP_PlGF2 (Supplementary Table 5), signifying electrostatically-driven assembly. The formation of compact monodisperse nanocomplexes was confirmed by DLS measurements, which showed an increase of 3 nm in the hydrodynamic diameter after S^- binding (Fig. 2b). This was further supported by SR–SAXS, which revealed a concomitant increase in D_{max} (*ca.* 1 nm; Fig. 2c) and R_g (*ca.* 9 Å; Supplementary Table 4) after polymer surfactant addition, and a further decrease in the Porod exponent (P_E), likely arising from the presence of the flexible polymer surfactant chains (Supplementary Table 4). The SR–SAXS data were also used for *ab initio* bead modelling, which gave a discrete, globular, [S⁻]scGFP_PlGF2 structure that was larger than scGFP_PIGF2, and consistent with the fusion protein surrounded by the S^- polymer surfactant corona (Fig. 2f and Supplementary Figure 7).

2.3. Nanocomplex assembly at the stem cell plasma membrane

Both the [S⁻]scGFP_PlGF2 nanocomplex and the scGFP_PIGF2 precursor were not cytotoxic to hMSCs below incubation concentrations of 12 μM (Supplementary Figure 8 and 9). Accordingly, all subsequent cell experiments were performed at 4 μM, which did not inhibit hMSC proliferation with either construct (Supplementary Figure 10). Flow cytometry studies revealed a labelling efficiency of 100% for hMSCs modified with [S⁻]scGFP_PlGF2 or scGFP_PlGF2 after one day (Supplementary Figure 11 and 12), which decayed over a ten-day period (Supplementary Figure 13). Live cell confocal fluorescence microscopy imaging confirmed that both [S⁻]scGFP_PlGF2 and scGFP_PlGF2 strongly associated with the hMSC plasma membrane after incubation (Fig. 3), where the supercationic scGFP_PlGF2 likely interacted *via* electrostatic interactions with anionic sulfated proteoglycans [45], while [S⁻]scGFP_PlGF2 through membrane bilayer intercalation by the nonylphenol tails of the protein-bound polymer surfactant corona (Fig. 1) [35,44]. Time-lapse widefield fluorescence microscopy showed rapid uptake of the scGFP_PlGF2 by the hMSCs, which was less evident with the [S⁻]scGFP_PlGF2 nanocomplex (Supplementary Figure 14). This is due to the hydrophobic nature of the nanocomplex-cell membrane interaction rather than the coulombic interaction that occurs between the scGFP moiety, as seen in previous studies [35–37]. Furthermore, an anti-GFP antibody was used to quantify the bound nanocomplex or scGFP_PlGF2 to the stem cell plasma membrane, revealing the presence of the nanocomplex on the membrane for up to 24 h (Supplementary Figure 15).

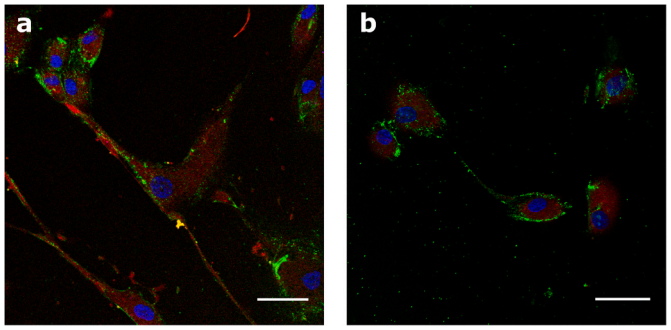

Fig. 3. Live cell confocal images of human mesenchymal stem cells (hMSCs) after modification with the constructs. hMSCs were treated with either **a** scGFP_PlGF2 (green) or **b** [S⁻]scGFP_PlGF2 (green) for 15 min at 37 °C and were imaged immediately after exposure. Cell nuclei were stained with Hoechst (blue) and cytoplasm was stained with a cell tracker (red). Scale bar = 50 μm. (For interpretation of the references to colour in this figure legend, the reader is referred to the Web version of this article.)

This indicated that the mode of interaction with the plasma membrane, *i.e.*, charge vs hydrophobic insertion, impacted significantly on the rate of internalisation, potentially through an endocytic mechanism. The rapid endocytosis of supercharged proteins is well documented and has been actively utilised to develop novel transfection vectors and to promote tissue penetration of proteins [45–47]. Moreover, our previous studies using supercharged protein-polymer surfactant conjugates have indicated a clathrin-mediated endocytotic mechanism for both supercharged proteins and their respective conjugates [35,37].

In order to estimate the number of constructs per cell, incubation solution depletion experiments were performed over a range of protein concentrations (Supplementary Figure 16). As the incubation concentration was increased, both scGFP_PlGF2 and [S⁻]scGFP_PlGF2 showed a steady increase in the number of constructs per cell that appeared to plateau at approximately 7.6 and 3.5 billion per cell, respectively. By considering the average cell plasma membrane area, this equated to 5 and 2.5 layers of scGFP_PlGF2 and [S⁻]scGFP_PlGF2 per cell, respectively, which is indicative of strong protein-protein interactions leading to self-assembly at the membrane. Indeed, our previous work has shown that chemically supercharged proteins can undergo hierarchical self-assemble *in vitro* via a partial charge neutralisation process [48–50].

The multipotency of the hMSCs was not supressed by the introduction of scGFP_PlGF2 or [S⁻]scGFP_PlGF2 to the plasma membrane. The hMSCs could still undergo osteogenesis (Alizarin red S stain and *runx2* mRNA expression; Supplementary Figure 17) or adipogenesis (Oil red O stain and *pparg* mRNA expression; Supplementary Figure 18) and the process was not observably or statistically different when compared to the untreated cell controls, respectively. Surprisingly, for experiments conducted in chondrogenic differentiation media, the transcription of the chondrogenesis marker gene *col2a1* was upregulated for hMSCs modified with [S⁻]scGFP_PlGF2 (Supplementary Figure 19). It is possible that this increased chondrogenic differentiation potential may have resulted from a reduction in the oxygen transport into the cells arising from the membrane coating, as hypoxic environments have been shown to drive chondrogenesis [51]. Additionally, *sox9* was upregulated while collagen X was only negligible, indicating that all cells were committed to chondrogenic differentiation. However, as stem cells are extremely sensitive to their chemical and physical microenvironments, there are a plethora of other factors that may have contributed to this observation.

2.4. The effect of hMSC membrane re-engineering on collagen type II affinity

Collagen II comprises 95% of articular cartilage [52]. Accordingly, the ability of [S⁻]scGFP_PlGF2 and scGFP_PlGF2 functionalised hMSCs

to adhere to collagen II was evaluated using a static adhesion assay. Suspensions of modified hMSCs were incubated in well-plates coated with either collagen II or bovine serum albumin (BSA) and the number of adherent hMSCs was evaluated by measuring the DNA content of each well. Importantly, there was a significant increase in the number of [S$^-$] scGFP_PlGF2 modified cells bound to the collagen II substrate when compared with either the unmodified control or the scGFP_PlGF2 precursor (Fig. 4a). This increased adhesion was attributed to the longer persistence time of the nanocomplex on the plasma membrane, when compared to the scGFP_PlGF2, which was internalised rapidly. Moreover, the orientation and hence the steric accessibility of the peptide in the scGFP_PlGF2 modified cells may have been reduced, as PlGF2 can bind to the neuropilin-1 (CD304) receptor present in low amounts on hMSCs, changing the orientation of the protein to allow the scGFP moiety face the ECM [53,54]. This different orientation is likely prevented by the predominant surfactant hydrophobic anchoring to the cell membrane, making the PlGF2 domain face the surrounding available to interact with the ECM proteins.

Additionally, the adhesiveness to non-cartilaginous intra-articular tissue, collagen I was also tested in static conditions, with no significant increase in hMSC adhesion after modification using scGFP_PlGF2 or [S$^-$] scGFP_PlGF2 (Supplementary Figure 20).

Dynamic cell adhesion experiments to collagen II were also performed under flow using a microfluidics chip to simulate the low shear stresses experienced in the synovium of the knee joint [55–57]. Adhesion experiments performed at 0.75, 1.0 and 1.5 dyne cm^{-2} all showed an increase in adhesion of hMSC modified with [S$^-$]scGFP_PlGF2 to collagen II, which was not apparent for the scGFP_PlGF2 modified cells (Fig. 4b–d). These data, along with the those generated using the static adhesion system, support a scenario where the PlGF2 peptide is addressable and can therefore bind to collagen II when presented on the surface of the hMSC using the [S$^-$]scGFP_PlGF2 nanocomplex.

2.5. Adhesion of modified hMSCs to cartilage ex vivo explants

To investigate the ability of the nanocomplex-modified hMSCs to bind to living AC, 6 mm bovine *ex vivo* articular explants from the lateral and patellar groove of 6–8 weekold calves were harvested 8 h post-mortem (see Experimental section 4.18). Bovine living explants are currently recognised as one of the best available models to represent articular cartilage [58]. Here, [S$^-$]scGFP_PlGF2-modified hMSCs in suspension (see Experimental section 4.11) were introduced to the cartilage explant substrates and left to adhere for 4 h before washing twice with PBS to remove unbound cells and treated for electron or light microscopy (see Experimental section 4.19 and 4.20). Significantly, scanning electron micrographs of the cartilage surface revealed that the [S$^-$]scGFP_PlGF2-modified hMSCs remained in greater numbers, when compared to the hMSC controls (Fig. 5a and b), which indicated increased adhesion to the articular surface. Moreover, fluorescence microscopy imaging of histology slices taken from *ex vivo* explants incubated for 4 h with the nanocomplex-modified hMSCs revealed a high concentration of the cells at the cartilage-media interface even after

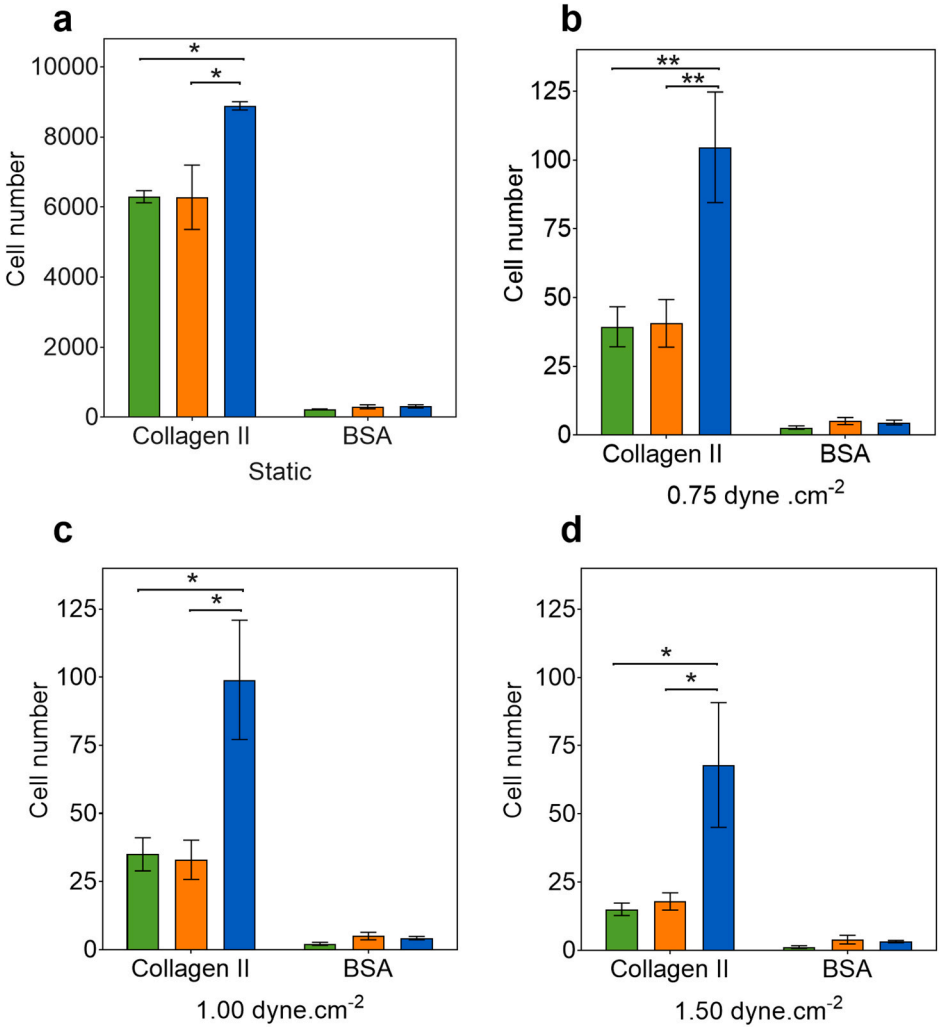

Fig. 4. Static and dynamic affinity assays. **a** Static affinity assay showing the human mesenchymal stem cells (hMSCs) adherence to immobilised collagen II after hMSCs were treated with 4 μM of either scGFP_PlGF2 (orange bars) or [S$^-$] scGFP_PlGF2 (blue bars) for 15 min, compared to the untreated cell controls (green bars). hMSCs were suspended in DMEM phenol free media without any supplements. The cells were added to the wells pre-coated with collagen type II (0.2 mg mL^{-1}) or bovine serum albumin (BSA, 10 mg mL^{-1}), and incubated for 4 h at 37 °C in a 5% CO_2 atmosphere. Cell attachment was measured by DNA quantification. Average represented as bars with standard deviation calculated using hMSCs from 4 different patients (n = 4). Dynamic affinity assay showing the hMSCs adherence to collagen II under shear at **b** 0.75 dyne cm^{-2}, **c** 1.00 dyne cm^{-2}, and **d** 1.5 dyne cm^{-2}. The cells were added at a density of 10^6 cells per mL in serum-free media into a reservoir in a VenaFluoro8 biochip coated with collagen type II (0.2 mg mL^{-1}), and bovine serum albumin (BSA, 0.1 mg mL^{-1}). Average represented as bars with standard deviation calculated using hMSCs from 3 different patients (n = 3). Comparison of differences was tested using an unpaired student t-test with a p-value < 0.05 and 0.01 considered significant (*) and highly significant (**) respectively. (For interpretation of the references to colour in this figure legend, the reader is referred to the Web version of this article.)

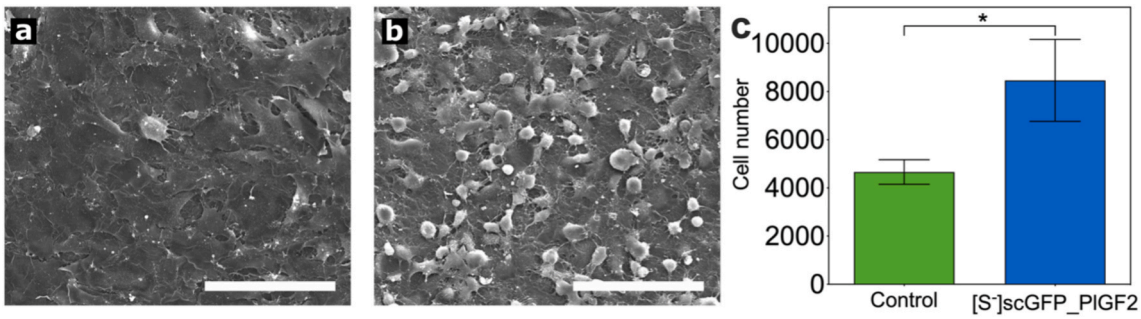

Fig. 5. Scanning electron microscopy images of human mesenchymal stem cells (hMSCs) on bovine explant surface. hMSCs were used unlabelled (**a**) or treated with 4 μM of [S⁻]scGFP_PlGF2 for 15 min (**b**), then seeded on bovine explant discs of 6 mm diameter and allowed to attach for 4 h at 37 °C in a 5% CO_2 atmosphere in serum-free media. Samples were fixed, treated with osmium to improve contrast, dehydrated with ethanol, and coated with gold/palladium. **b** untreated hMSCs were taken as a control. **c** Adhesion assay in bovine *ex vivo* explants. hMSCs were treated for 15 min with [S⁻]scGFP_PlGF2 (blue), using untreated cells as a control (green). hMSCs were suspended in DMEM phenol-free media without any supplements and added to 96-well plates containing 6 mm diameter living bovine explant discs. Cells were allowed to attach for 4 h at 37 °C in a 5% CO_2 atmosphere. The explants were then imaged using confocal fluorescence microscopy, taking three-dimensional images in six random places, and the images were flattened and analysed using Fiji software. Average represented as bars with standard deviation calculated using 6 cartilage discs (n = 6). Comparison of differences was tested using an unpaired student t-test with a p-value < 0.05 and 0.01 considered significant (*) and highly significant (**) respectively, compared to control. Scale bar = 100 μm. (For interpretation of the references to colour in this figure legend, the reader is referred to the Web version of this article.)

rinsing non-adherent cells and imaged after 24 h (Supplementary Figure 21). Semi-quantitative image analysis from confocal fluorescent images was also performed on the living cartilage explants after the addition of the nanocomplex modified hMSCs (Fig. 5c and Supplementary Figure 22). Significantly, when seeded onto the *ex vivo* bovine cartilage explants, the number of adhered hMSCs was two-fold higher after [S⁻]scGFP_PlGF2 functionalisation, when compared with the unmodified cell controls (Fig. 5c).

The ability of the free nanocomplex, the scGFP_PlGF2 precursor, and scGFP to directly interact with chondrocytes within the *ex vivo* articular

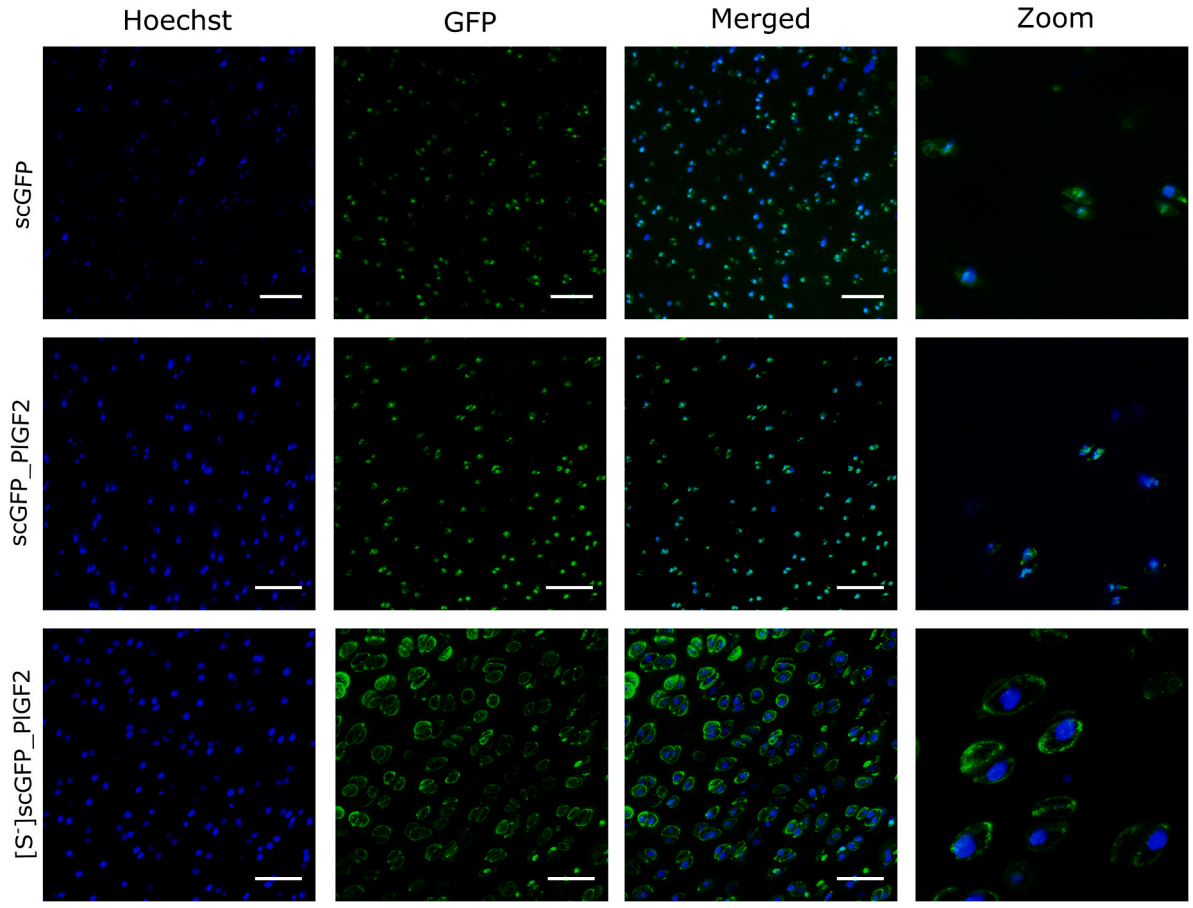

Fig. 6. Bovine cartilage *ex vivo* explants discs directly exposed to the constructs. Discs were incubated in 1 μM solution of either scGFP (green, upper row), scGFP_PlGF2 (green, middle row), or [S⁻]scGFP_PlGF2 (green, bottom row), respectively, with 1% bovine serum albumin. The cross sections were imaged after 24 h. Cell nuclei were stained with DAPI (blue). Scale bar = 100 μm. (For interpretation of the references to colour in this figure legend, the reader is referred to the Web version of this article.)

explants was also explored (Supplementary Figure 23). Previous reports have indicated that the degree and distribution of supercharging on a protein surface directly impacts on cartilage ECM penetration and distribution [59]. Moreover, recent studies have employed antibody-PlGF2 fusions to improve adhesion in *ex vivo* collagen sheets [60]. All three constructs were able to interact with the explant substrates. The [S$^-$] scGFP_PlGF2 nanocomplexexhibited a strong interaction with the chondrocyte plasma membrane, with little evidence of endocytosis (Fig. 6).

Conversely, both scGFP and scGFP_PlGF2 were rapidly internalised by the chondrocytes (Fig. 6), which signified that the magnitude of the affinity of the PlGF2 peptide for the ECM was overcome by active endocytosis of the highly supercharged protein. Indeed, the rapid processing of the unconjugated protein constructs was reflected in supernatant depletion experiments, which showed a greater uptake of scGFP and scGFP_PlGF2 (cf. [S$^-$]scGFP_PlGF2; Supplementary Figure 24), and corroborates the charge-dependence resulting from the coulombic attraction between the negatively charged cell membranes or ECM components and the positive charge of the scGFP moiety [59]. Furthermore, these results highlight the further utility of the scGFP systems and the importance of the surfactant in the nanocomplex, as it avoids aggregation, and it is retained on the ECM.

3. Conclusion

In this study, we demonstrated that hMSCs could be augmented with an artificial membrane binding nanocomplex to improve cartilage adhesion performance. This was achieved by harnessing the inherent ECM-binding affinity of a growth factor-derived peptide sequence, which could be readily displayed on the surface of hMSCs in high numbers and with sufficient duration. The hMSC membrane re-engineering protocol is facile and did not affect cell viability, proliferation, or differentiation. Importantly, hMSC adhesion to a key ECM component of cartilage, collagen II, was improved, as was the cell affinity for AC explants, despite the presence of endogenous anti-adhesive molecules.

Comparison of the analogues [S$^-$]scGFP_PlGF2 nanocomplex and scGFP_PlGF2 protein revealed the importance of the surfactant corona on the protein, for instance, lower cytotoxicity, longer retention on the membrane, as well as enhanced adhesion under static and dynamic conditions to collagen II, the main component of hyaline cartilage.

Our results support a mechanism whereby hydrophobic interactions drive [S$^-$]scGFP_PlGF2 association at the plasma membrane, promoting an end-on insertion of the scGFP motif [35,37,44], which is critical for effective binding of the PlGF2 peptide to the AC ECM proteins. Moreover, the nanocomplex membrane persistence (days) and number (*ca.* 3.5 billion per cell) could help overcome the rapid loss of viable therapeutic cells at the site of injury through *anoikis* and incorrect targeting [21]. Indeed, the lack of viable transplanted cells is clearly a challenge across a range of stem cell therapies, and several genetic engineering approaches have been developed to improve hMSC performance (viability, mobility and proliferation) in injury environments [61]. When compared to these approaches, which have high costs and potential side-effects subject to insertional oncogenesis [62], our approach leverages transient and potentially tuneable membrane display, the ability to plug in to existing cell manufacturing processes, and scalable protein production. Moreover, our simple one step cell membrane modification methodology is cell agnostic and could be readily extended to other therapeutic cell types (e.g., pluripotent stem cells or epithelial cells, etc.). It is our hope that these emerging cell therapy technologies will improve the efficacy of injectable stem cell treatments to drive clinical translation. Indeed, the next stage of the development of these artificial membrane binding nanocomplexes will involve generating compelling cartilage regeneration *in vivo* preclinical animal model data.

4. Experimental

4.1. scGFP_PlGF2 construct design, expression, and purification

The plasmid with sequence N-His6-scGFP-PlGF2-C (Supplementary Tables 1 and 2) was designed for pOPIN F vector1 (Oxford Protein Production Facility; Addgene plasmid # 26,042), which is enhanced for multi-histidine tag purification under control of the lac-operon and designed for ampicillin resistance. The polymerase chain reaction (PCR) was used to amplify the gene sequence. A mix of 1 μM template scGFP-PlGF2, forward and reverse primers (each at 1 μM), 5 U μL^{-1} of polymerase Labtaq Hi-Fidelity Polymerase™ (LabTech, UK) and reaction buffer 5x (LabTech, UK), plus DNase free water to make a final volume of 50 μL, was added to a DNAse free 200 μL tube. This was subjected to PCR in a thermocycler (Thermo Fisher Scientific, UK) with the following settings: 95 °C for 5 min for initialization and heat activation of the DNA polymerases, 95 °C 30 s for denaturation at the beginning of each cycle, 62 °C 30 s, 72 °C 3 min, 90 °C to 2 °C for 30 cycles, 72 °C for 10 min, and finally cooled at 4 °C. A 1.5% w/v agarose gel and stained with SYBR safe stain (Invitrogen, UK) to facilitate the separation and purification of the PCR products. For extraction, a QIAquick gel extraction kit was used as indicated by the manufacturer.

For linearization, the vector (80 mg mL^{-1}) was added to cut smart buffer, 1 unit of restriction enzyme Hind III, 1 unit of Kpn I (New England BioLabs, UK), and nuclease-free water. The mixture incubated overnight at 37 °C. The sample mixture was then treated with a NucleoSpin Gel and PCR clean-up kit following the instruction of the manufacturer (Gmbg & Co. KG, Germany). The In-Fusion™ cloning method was used to insert the fusion gene into the linearized plasmid.

Transformation in Competent Stellar Cells™ (Clontech, UK) was performed according to the manufacturer's instructions. In summary, the In-Fusion™ mixture was added to Competent Stellar Cells™ , gently mixed, and then submitted to heat shock transformation for 45 s at 42 °C before being incubated in on ice. Subsequently, Super Optimal broth with Catabolite repression (SOC) medium was added before the cell suspension was incubated for 1 h at 37 °C. The cell suspension was then centrifuged at 12,000 g for 10 min, resuspended in 50 μL of SOC medium, and was homogeneously distributed into LB agar plates containing carbenicillin (5 μg mL^{-1}). A single colony was selected from the LB agar plate and used to inoculate starter culture (Lysogenic broth with added carbenicillin 5 μg mL^{-1}), and left in rotating motion incubator at 200 rpm over night at 37 °C. For plasmid DNA isolation and purification, a QIAgen Spin Miniprep kit was used according to the manufacturer's instructions. For transformation in BL21 cells, an aliquot of purified plasmid scgfp-plgf2_123–144 (>100 ng mL^{-1}) was added to competent BL21 DE3 *Escherichia coli* (*E. coli*) cells (New England BioLabs, UK) and equilibrated on ice for 30 min. Heat shock was performed in a water bath at 42 °C for 10 s. The cell suspension was then equilibrated on ice for 5 min before the addition of 950 μL of SOC media. The suspension was incubated for 60 min in shaking incubator at 200 rpm at 37 °C. The resulting mixture was centrifuged at 120 g for 5 min, and the supernatant was discarded. The cell pellet was resuspended in 50 μL of SOC medium and the suspension was used to inoculate freshly made LB agar plates, and incubated overnight at 37 °C.

The gene sequence scgfp-plgf2_123–144 or scgfp was expressed using competent BL21 (DE3) *E. coli* cells. A single colony was chosen to inoculate autoclaved LB broth, containing carbenicillin (5 μg mL^{-1}) and incubated overnight at 37 °C rotating at 200 rpm. The cell suspension was then added to 1 L of autoclaved LB medium with 5 μg mL^{-1} carbenicillin and stirred at 200 rpm at 37 °C for approximately 4 h, until the optical density reached 0.6–0.8 (λ = 600 nm). Protein expression was induced using a final concentration of 10 mM of isopropylthiogalactosidase (IPTG; Apollo Scientific, Japan) and the cell suspension was incubated and agitated overnight at 200 rpm at 37 °C. The culture was centrifuged at 4000 g for 35 min at 4 °C, and the sediment was resuspended in lysis buffer (20 mM Tris HCl, 1 M NaCl and

20 mM imidazole at pH 7.5). Cells were lysed by sonication using a Vibra Cell VCX 1500 (Sonics & Materials, USA) at a 63% amplitude. Phylmethylsulfonyl fluoride (PMSF) solution (100 mM PMSF in dimethyl sulfoxide DMSO) was added before and after sonication, along with a sufficient amount of lyophilised DNase I from bovine pancreas. The lysed sample was centrifuged at 20,000 g for 30 min, the supernatant was filtered through a 0.22 μm cellulose membrane syringe filter and purified by immobilised metal affinity chromatography using nickel nitrilotriacetic acid (Ni-NTA) as the immobile phase. Using a XK 16 column (GE healthcare life sciences, UK) containing 25 mL of Ni-NTA (Qiagen, UK). The column was washed with lysis buffer and increasing gradients of imidazole using ÄKTA purifier (GE Healthcare, UK) until eluted with high imidazole buffer (500 mM Tris HCl, 1 M NaCl and 20 mM Imidazole adjusted to pH 7.5 with concentrated HCl). The resulting purified protein was buffer exchanged into working buffer (400 mM NaCl, 20 mM Tris HCl, pH 7.5) using 14,000 MWCO cellulose dialysis tubing, (Fisher scientific, US) at 4 °C. The same method was used to purify scGFP.

4.2. Polyacrylamide gel electrophoresis (SDS-PAGE)

10 μL sample aliquots containing SAB (5% SDS, 50 mM ethylendiaminetetraacetic acid (EDTA), 0.5 mM Tris and 7 mM β- mercaptoethanol and bromophenol was added until dark blue) were denatured at 95 °C for 5 min. A 4–20% bis-tris gel (Invitrogen, USA) was submerged into an X-Cell Surelock electrophoresis chamber (Thermo Fisher, UK) containing running buffer (50 mM Tris base, 38.5 mM glycine and 7 mM SDS). 10 μL of the denatured sample was added to each well, using a PageRuler Plus Prestained ladder (Thermo Fisher, UK) 10–180 kDa as reference. Electrophoresis was performed using a continuous voltage of 200 V to the system for 60 min. The gel was removed from the cast and stained with Coomassie Blue™ and distained using solution containing 20% ethanol and 5% acetic acid for up to 2 h.

4.3. Bicinchoninic acid (BCA)

A Pierce BCA Protein Assay™ kit (Thermo Fisher scientific, UK) was used for this process. A stock solution for the working reagent (WR) was prepared according to the number of samples (200 μL of WR in a 96 well plate). This was prepared by mixing reagent A ([2,2′-Biquinoline]-4,4′-dicarboxylic acid, sodium salt) and B (Copper II sulphate pentahydrate) in a 50 to 1 ratio. An aliquot of 25 μL of scGFP_PlGF2 in solution was added to a 96 well plate (Costar, UK), followed by the addition of 200 μL of WR to the same well. The plate was incubated at 37 °C for 30 min and the absorption was measured at 562 nm with a multi-mode plate reader Synergy neo2 (BioTek, USA). Known concentrations of bovine serum albumin (BSA) were used to produce a standard curve. The slope of the linear regression equation line from the plotted graph from absorbance at 562 nm against concentration was taken to produce a standard curve.

4.4. Matrix-assisted laser desorption/ionisation mass spectrometry time of flight (MALDI-TOF)

The average molecular weight of the protein constructs and polymer surfactants were obtained using a Bruker MALDI mass spectrometer (Applied Biosystems, UK) running FLEX control software (Bruker, USA). The sample was prepared using 1:1 ratio of cinnamic acid matrix (50:50 solution of acetonitrile and 0.1% TFA and saturate with α-Cyano-4-hydroxycinnamic acid), spotted 1 μL sample on rough steel plate and let dry at room temperature for 10 min before loading into the machine. Spectra were taken between 10 and 55 kDa for proteins and 0–5 kDa for surfactants.

4.5. Protein-polymer surfactant nanocomplex [S$^-$]scGFP_PlGF2 formation

To form the nanocomplex [S$^-$]scGFP_PlGF2, the concentration of the protein scGFP_PlGF2 was evaluated using UV–vis light absorbance at 280 and 487 nm over the wavelength range 200–600 nm. Beer-Lambert law was used to calculate the protein concentration where A is the absorbance at a wavelength of 280 nm and ε is the extinction coefficient, 17,330 $M^{-1}cm^{-1}$ at 280 nm (Protein Calculator, RCSB Protein Data Bank). For fluorescence Spectroscopy, samples were analysed using a fluorescence spectrometer in Cary Eclipse fluorometer (Agilent Technologies, USA) using Cary Scan (Agilent Technologies, USA) software. Excitation and emission scans were performed from 350 to 600 nm. The surfactant was added in a ratio of 1.4 to 1 of surfactant molecules to positive sites, respectively. The solution was stirred overnight at 200 rpm and it was then dialysed in a 14,000 MWCO cellulose bag into 400 mM NaCl and 20 mM Tris at pH 7.5.

4.6. Synchrotron radiation circular dichroism

Synchrotron radiation circular dichroism (SR–CD) was performed at Diamond Light Source (Oxford, UK) on the B23 beamline. Spectra were measured from 180 to 260 nm, using a cylindrical cell with a 200 μm pathlength in a Linkam System. The beam current was 300 mA, the slit width was 1 mm, and the integration time was 2 s. The CD spectra were obtained over a temperature range of 24–90 °C with a measurement at every 3°, and an equilibration time of 1 min per measurement. The resulting data were analysed and deconvoluted using BestSel Software [63], which trimmed the spectra to 190–250 nm and assessed the secondary structure features in this range. Particularly, this software considers the existing twist in beta-structures and can differentiate between parallel and antiparallel beta sheets reliably to accurately predict the secondary structure over a wide range of proteins and is optimised for spectra obtained from SR–CD. The algorithm works with data taken from 175 nm and as accurately with data obtained from 190 nm. Protein samples were measured at concentrations between 3 and 3.6 mg mL^{-1} in 20 mM sodium phosphate buffer pH 7.5.

4.7. Dynamic light scattering (DLS) and zeta potentiometry

DLS and zeta potentiometry were performed using a ZetaSizer Nano ZS (Malvern Instruments, UK) and ZetaSizer software (Malvern Instruments, UK). Samples were filtered (0.22 μm pore size) before measurement, the parameters selected were 3 runs with 10 measurements each with 120 s of equilibration time.

4.8. Protein structure modelling via iterative threading assembly simulations (I-TASSER)

The input of the I-TASSER (https://zhanglab.ccmb.med.umich.edu/I-TASSER/) structure prediction server was the scGFP_PIGF2 amino acid sequence (Supplementary table 2), with chain A of the crystal structure of superfolder GFP (PDBID: 2B3P:A) specified as a template [40,41].

4.9. Synchrotron radiation small angle X-ray scattering (SR–SAXS)

SR–SAXS measurements were performed using the Diamond Light Source (Oxford, UK) mail-in service on beamline B21. The detector (Eiger 4 M) was used with a range from 0.0032 to 0.38 $Å^{-1}$. The beam size was <75 μm, operating with a fixed camera length at 4.014 m at 12.4 keV. SR–SAXS measurements were coupled with size exclusion chromatography (SEC–SAXS) using a superdex 200 column (GE Healthcare). The data was collected in 30 successive frames, each with a 1 s exposure time. The 60 μL samples at 4 mg mL^{-1} were prepared by concentrating the purified constructs with a 10 MWCO spin concentrator (Merck, USA) until the desired concentration was achieved, and

verified with NanoDrop ND-1000 (Thermo Scientific, USA). The data were scaled, merged, and background subtracted buffer using ScÅtter software. This same software was also used to determine the Porod exponent (P_E; the slope of a line of linear regression to the scattering data in the Porod–Debye region) [64] and to convert the data to real space distributions for further analysis with ATSAS plugins [65]. Briefly, a Fourier inversion was performed on the scattering data ($I(q)$; equation 1) to determine the pair-distance distribution function ($P(r)$), from which the radius of gyration (R_g), maximum dimension (D_{max}), and the radial average (r) could be determined using ScÅtter software. Porod exponent. The output from ScÅtter was submitted to EMBL DAMMIF online service [66] in order to obtain a dummy atom bead model. Dummy atom bead models were fitted to the predicted 3-dimensional structure determined from I-TASSER (see Experimental section 4.8).

$$P(r) = \frac{1}{2\pi^2} \int_0^\infty I(q) \cdot qr \cdot \sin(qr) \cdot dq$$

Equation 1. Fourier inversion of the scattering curve I(q) to obtain the pair-distance distribution function ($P(r)$).

4.10. Human mesenchymal stem cell culture and membrane modification

Human mesenchymal stem cells (hMSCs) were isolated from the proximal femur bone marrow of patients undergoing total hip replacement surgery, according with the Bristol Southmead Hospital Research Ethics Committee guidelines (reference #078/01). All cell culture work was executed in SAFE 2020 laminar flow hoods (Thermo Fisher Scientific, UK), and incubated in Hera cell 150 (Thermo Fisher Scientific, UK) at 37 °C under a 5% carbon dioxide atmosphere. hMSCs were expanded in monolayer using T25, T75 or T175 flasks (Fisher Scientific, UK) using 5, 12, or 25 mL of culture medium respectively. The media was changed every 2 days. The hMSCs were expanded in complete media: DMEM containing $NaHCO_3$, supplemented with 100 units·mL^{-1} penicillin, 100 μg mL^{-1} streptomycin, 2 mM GlutaMAX supplement (Invitrogen, USA), 10% v/v foetal bovine serum (FBS), and 5 ng mL^{-1} of freshly added basic human fibroblast growth factors (FGF) (Peprotech, USA).

4.11. Stem cell modification with nanocomplexes

For membrane modification, hMSCs were seeded in well plates at desired density, and after adhesion to the plate, were incubated for 15 and 30 min with 2 mL of scGFP_PlGF2 or [S$^-$]scGFP_PlGF2 and monitored using widefield fluorescent microscopy (Leica LASX). As there was no observable difference in the fluorescence intensity between the cells treated for 15 or 30 min, an incubation time for 15 min used for all further experiments. hMSCs were also modified in suspension. Here, after trypsinisation and resuspension in phenol-free DMEM (without supplements), cells were incubated for 15 min at 37 °C with 2 mL of 4 μM of either scGFP_PlGF2 or [S$^-$]scGFP_PlGF2 with agitation at 50 rpm. The hMSCs suspension was centrifuged at 220 g for 5 min to remove unbound constructs and resuspended in phenol-free DMEM without supplements at desired density.

4.12. Cell metabolic activity and proliferation

An MTS colorimetric assay CellTiter 96 kit (Promega, USA) was used to measure the total metabolic rate of hMSCs as an indication of viability. hMSCs in monolayer were exposed to a range of different concentrations of scGFP_PlGF2 and [S$^-$]scGFP_PlGF2 (2, 4, 6, 12 and 18 μM) in triplicate for 15 min at 37 °C. The same principle was applied to measure the metabolic activity of hMSCs after being exposed for 15 min to different concentrations (0.5, 2, 4, and 10 mg mL^{-1}) of free oxidised IGEPAL co-890. These concentrations were equivalent to the conjugated surfactant concentration in [S$^-$]scGFP_PlGF2, e.g. for a protein concentration of 2.75 μM, 0.5 mg mL^{-1} of surfactant was added to form the nanocomplex. The absorbance of formazan was measured at 490 nm after 2 h using microplate Mithras LB 140 (Berthold technologies, Germany). For cell proliferation, hMSCs were suspended in phenol-free DMEM (without supplements) and treated for 15 min at 37 °C with 2 mL of 4 μM of scGFP_PlGF2 and [S$^-$]scGFP_PlGF2 with agitation at 50 rpm. Cells were separated from unbound constructs by centrifugation at 220g or 5 and resuspended in phenol-free DMEM without supplements and counted. 100,000 cells were seeded in a T25 flask with 5 mL of culture medium containing 5 ng mL^{-1} of FGF. The medium was changed every two days. After seven days, cells were harvested, counted, and seeded at the initial density.

4.13. Flow cytometry

hMSCs were resuspended in DMEM phenol-free medium and exposed to 2 mL of 4 μM scGFP_PlGF2 or [S$^-$]scGFP_PlGF2 for 15 min inside an incubator at 37 °C with agitation at 50 rpm. The cell suspension was centrifuged at 220 g for 5 min and the pellet resuspended in flow cytometry buffer (2% v/v FBS, 2.5 mM EDTA in PBS), at 1 × 10^6 cells per mL with 0.004 mg mL^{-1} of propidium iodide (PI). The cell suspension was transferred to flow cytometry tubes (VWR, UK). Samples were analysed with NovoCyte flow cytometer (ACEA Biosciences, USA) and analysed using NovoExpress software (ACEA Biosciences, USA). Parameters were set to 100–300 events per second with 20,000 events accumulated for gate analysis. Untreated cells were used to define the four gates as follows: whole cells by forward scatter height (FSC–H) vs side scatter height (SSC–H), single cells by forward scatter area (FSC-A) vs (FSC–H), PI negative living cells by FSC-A vs Qdot605A and positively labelled cells with GFP were defined by FITC-A vs FSC-A.

To quantify the amount of scGFP_PlGF2 or nanocomplex on the surface of the cells, an anti-GFP antibody (Biolegend, UK), with an APC fluorophore (Ex/Em = 650/660 nm) was used for co-localisation. hMSCs were seeded at a density of 50,000 cells per well and exposed to 2 mL of 4 μM scGFP_PlGF2 or [S$^-$]scGFP_PlGF2 for 15 min inside an incubator at 37 °C. The modified hMSCs were detached using trypsin/EDTA solution for 5 min at 37 °C, rinsed with complete DMEM containing serum, transferred to 14 cm flow cytometry tubes and rinsed with PBS. The supernatant was discarded, and 100 μL of a 1:50 antibody solution in PBS was added to the cells and gently mixed using a pipette. The cell suspension was incubated at 4 °C for 20 min and 2 mL of PBS were added to each tube. The solution was centrifuged at 220 g for 5 min and the cells were resuspended in 100 μL of PBS and submitted for flow cytometry quantification immediately using MACSQUANT X (Miltenyi, Germany) instrument. The data was analysed using FlowJo software. Parameters were set to 100–300 events per second taking 80 μL of solution every time. Untreated cells labelled with the anti-GFP antibody were used to define the gates as follows: whole cells by forward scatter height (FSC–H) vs side scatter height (SSC–H), single cells by forward scatter area (FSC-A) vs (FSC–H), positively labelled cells with GFP were defined by FITC-A vs SSC-A, and antibody labelled cells were defined by APC-A vs SSC-A. The median fluorescence intensity of the APC gate was taken to graph the results.

4.14. Evaluating the average number of constructs per cell

hMSCs were seeded at a density of 20,000 cell per well and treated with 0.25, 0.5, 2, 4 and 6 μM solutions of scGFP_PlGF2 or [S$^-$] scGFP_PlGF2 for 15 min at 37 °C in an incubator. The supernatant was aspirated and collected for UV–vis analysis, taking a full spectrum from 200 to 600 nm. The absorption intensity at 487 nm was compared to the known initial absorption and the number of biohybrid constructs on the surface of hMSCs was estimated through the reduction in total construct in the supernatant.

4.15. Live cell light microscopy

For confocal fluorescence microscopy (Leica SP8), 40,000 hMSCs were seeded in glass bottom micro well dishes 35 mm (MatTek, USA) with culture media and allowed to adhere overnight. The nucleus was stained with of Hoechst 33,342 (Fisher scientific H3570) and the cytoplasm using of Cell Tracker red CMTPX dye (Life technologies C34552) for 30 min at 37 °C under 5% CO_2 atmosphere. This media was then aspirated and replaced with 2 mL of 4 μM of sample scGFP_PlGF2 or [S^-] scGFP_PlGF2. Cells were incubated for 15 min, washed twice with 1 mL of PBS, and then immersed in 2 mL of complete phenol-free medium.

For time lapse widefield fluorescence microscopy, hMSCs were seeded at a density of 20,000 cells per well, in tissue cultured treated 6 well plate 34.8 mm (Corning, UK) with supplemented culture media 24 h previous to the experiment. The nucleus was stained with Hoechst 33,342 (Fisher scientific H3570) for 20 min at 37 °C under 5% CO_2 atmosphere. This media was then aspirated and replaced with 2 mL of 4 μM of sample scGFP_PlGF2 and [S^-]scGFP_PlGF2. Cells were incubated for 15 min, then washed twice with 1 mL of PBS. Finally, 2 mL of supplemented phenol-free medium DMEM was added. The cells were analysed using an inverted microscope (Leica LASX DMI6000) with a 20x lens at 37 °C under CO_2 atmosphere for 12 h, taking one image every 15 min.

4.16. hMSC differentiation staining and qPCR

For osteogenesis and adipogenesis differentiation, 20,000 hMSCs were seeded in a 12 well plate, using cells from three different patients. The cells were exposed to 300 μL of scGFP_PlGF2 or [S^-]scGFP_PlGF2 for 15 min and rinsed twice with PBS. The cells were cultured in StemPro™ Osteogenesis differentiation medium (Thermo Fisher Scientific, UK), StemPro™ Adipogenesis cell medium (Thermo Fisher Scientific, UK), or complete hMSC culture medium, with media changes every two days. Antifungal water (100 units of penicillin, 100 μg streptomycin and 2.5 μg of amphotericin in autoclaved dH_2O) was added to fill the remaining wells of the plate.

For osteocyte detection, sample wells were gently washed with 500 μL pf PBS twice, then cells were fixed with 4% paraformaldehyde (PFA) (BioLegend, USA) for 30 min at room temperature. The cell monolayer was washed with 500 μL of autoclaved dH_2O before adding 500 μL of filtered solution of Alizarin Red S (2% w/v Alizarin Red S, pH adjusted to 4.1 with HCl). The plate was incubated for 30 min at room temperature in the dark and washed four times with 1 mL of autoclaved dH_2O, and PBS was added prior to imaging. The samples were immediately imaged with a widefield inverted microscope and analysed with Fiji software (NIH, USA). All images were converted into a 16-bit image and a mean threshold was applied. Then, each image was submitted to particle analysis, using 0 to infinity size and 0 to 1 circularity for the total area covered by the stained monolayer.

For adipocyte detection, the medium was removed by pipetting and the sample wells were washed twice with 500 μL of PBS. 500 μL of neutral buffered formalin 10% (10% of 37–40 formaldehyde, 90% dH_2O, 33.5 mM sodium phosphate monobasic NaH_2PO_4, and 45.5 mM sodium phosphate dibasic Na_2HPO_4) to cover the cell monolayer, this was incubated at room temperature. After 45 min, fixation buffer was aspirated, and the wells were washed with 500 μL of autoclaved dH_2O followed by the addition of 500 μL of 60% isopropanol solution and incubated at room temperature for 5 min. The isopropanol was aspirated and Oil Red O staining solution (stock 0.3% Oil Red O in isopropanol, 3 parts diluted in 2 parts of autoclaved dH_2O) was added to fill the wells, filtering the solution right before staining. Cells were incubated for 30 min and the wells were washed several times with dH_2O. Images were taking using widefield inverted microscope.

For differentiation assays, cells from three different patients were seeded in a 6 well plate at a density of 50,000 cells. Cells were exposed to 1 mL of 4 μM of scGFP_PlGF2 or [S^-]scGFP_PlGF2 for 15 min in incubator at 37 °C. The wells were gently rinsed twice with 2 mL of PBS and then 2 mL of chondrogenesis media (4500 mg mL^{-1} glucose phenol-free DMEM containing pyridoxine-HCl and $NaHCO_3$, supplemented with 100 units·mL^{-1} penicillin and 100 μg mL^{-1} streptomycin, 2 mM GlutaMAX, 1 mM sodium pyruvate and 1% v/v insulin transferrin selenium ITS solution), freshly supplemented 0.01% v/v dexamethasone, 80 nML-ascorbic acid 2-phosphate, and 10 ng mL^{-1} of TGF-β3 (R&D Systems, USA), changing media every two days. The same principle was used for osteogenesis and adipogenesis, using StemPro prepared media and serum (Gibco, UK).

The cells were lysed to extract RNA with a Qiagen micro RNasy kit. The purified RNA was immediately processed for cDNA preparation, using a Takara PrimeScript RT reagent kit (Takara, Japan) according to the instructions provided by the manufacturer. This was performed in 200 μL RNase free PCR tubes, and the resulting mix was summited to PCR at 37 °C for 15 min, 85 °C 5 s and 4 °C for cooling. The resulting cDNA was immediately used or stored at −80 °C for future analysis. A MicroAmp Fast Optical 96-well reaction plate (Applied biosystems, UK) was used. On each well, 5.5 μL of a mixture containing 5 μL of Taqman master mix and 0.5 μL of the gene set were deposited on the left wall of the well. Followed by the addition of 1 μL cDNA of the sample with 3.5 μL of DNase-free water. The 96 well plate was covered with adhesive PCR plate film (Thermo Fisher Scientific, UK). qPCR was carried out using a QuantStudioTM 3D Digital PCR System (Life Technologies). The data obtained was analysed using the double delta Ct analysis method.

4.17. Static and dynamic hMSC collagen adhesion assays

For static adhesion measurements, a non-tissue culture treated 96 well plate (Fisher, UK) was used to assess adhesion of treated cells. 100 μL of either 0.2 mg mL^{-1} collagen II from bovine tracheal cartilage (Sigma C1188, UK), collagen I from rat tail, or 10 mg mL^{-1} BSA (control) was added to each well in triplicate and left at 4 °C overnight. The next day, wells were rinsed twice with 100 μL of PBS and non-specific binding sites were blocked with BSA solution 10 mg mL^{-1} for 1 h. hMSCs were counted and treated in suspension with either scGFP_PlGF2 or [S^-] scGFP_PlGF2. 10,000 cells were seeded in each well with 100 μL of DMEM phenol-free medium with no additives and incubated at 37 °C in a 5% CO_2 atmosphere. A standard curve was also made with different cell densities adding DMEM medium with all supplements in a tissue culture treated plate. After 4 h, the media was aspirated, and the wells were rinsed with 100 μL of PBS twice. DNA quantification assay (CyQUANT NF cell proliferation assay kit, Invitrogen) was performed, briefly, 100 μL of solution was added to each well and incubated for 60 min, fluorescence was measured with a microplate reader with excitation at 485 nm and emission at 530 nm.

Dynamic cell adhesion experiments were carried out with a Microfluidic pump ExiGo (Cellix Ltd, UK), with a shear stress precision of ±0.5%. All channels of the Vena8 Fluoro + biochip (Cellix Ltd, UK) were coated with 0.1 mg mL^{-1} collagen II from bovine tracheal cartilage (Sigma, UK) and left overnight at 4 °C in a humidified chamber. Non-specific sites were blocked with 10 μg mL^{-1} BSA. hMSCs were modified and resuspended at a density of 1×10^6 cells per mL in DMEM phenol-free medium without additives. Each channel was first washed with DMEM phenol-free medium with no additives for 30 s at 40 μL min^{-1}. Then, a 50 μL aliquot of cells modified with scGFP_PlGF2 and [S^-]scGFP_PlGF2 or unmodified cells, were added into the channel reservoir each time, and the suspension was withdrawn with a flow rate of 6, 4 and 3 mL min^{-1}. A real-time video of 10 s was recorded at 113 ms per frame at the five marked positions in the biochip, using (Leica LASX DMI6000). In the same way, Vena8 Fluoro + biochip (Cellix Ltd, UK) was coated with 10 μg mL^{-1} BSA to be used as a negative control.

4.18. Bovine ex vivo explants harvest and preparation

Cartilage explants were harvested form the lateral and patellar

groove of 6–8-week-old calves, obtained 6–8 h after death. The legs were carefully washed and disinfected with Rely + On Virkon (Dupont, UK) and warm dH_2O. The skin from the legs was carefully removed with 22-size surgical blades (Swann-Morton, UK) until the coronet to reveal the joint area. The hoofs and the top side of the leg were covered in aluminium foil and the exposed surface of the leg was sprayed with 70% ethanol in dH_2O and placed inside a laminar hood. The outer layer of tissue was removed to expose the articular cartilage, lateral and medial meniscus and to cut the anterior cruciate ligament. Cartilage disks from the lateral and patellar grove were delimited with an 8 mm biopsy punch (Stiefel, Germany) and carefully detached with a 22-size surgical scalpel (Swann-Morton, UK) and collected using tweezers (Supplementary Figure 23a). The discs were placed into falcon tubes in PBS containing 1% penicillin/streptomycin solution. After dissection, the pieces were placed in individual wells in a 48 well plate (Corning, UK) and kept in phenol-free medium fully supplemented with antibiotics.

Cartilage discs were washed twice in PBS before being cut to 6 mm diameter with a biopsy punch (Stiefel, Germany) and placed in a non-tissue culture treated 96 well plate (Fisher, UK) with 200 μL of DMEM phenol-free medium without supplements. Tissue discs were then stained with Hoechst nuclei stain for 5 min hMSCs were treated with [S^-]scGFP_PlGF2, and resuspended in DMEM phenol-free medium, using untreated cells as a control stained with CellTracker deep-red. hMSCs were counted and added onto the cartilage surface (20,000 cells) and placed in incubator at 37 °C with 5% CO_2 for 4 h. The samples were then used for confocal analysis, fixed for scanning electron microscopy SEM imaging or histology analysis.

4.19. Scanning electron microscopy and histology from bovine explants

All tissue samples were fixed with 2.5% glutaraldehyde for 1 h, and then were rinsed three times for 10 min with 100 mM sodium phosphate buffer pH 7.4. Cartilage samples were then placed in 1% osmium tetroxide for 1 h, and then washed three times for 10 min with 100 mM sodium phosphate buffer and washed with dH_2O for 10 min. Dehydrations steps were made with 25, 50, 70, 80, 90, 96, 100% ethanol before being processed with critical point dryer (CPD) Leica EM CPD300, set for 15 cycles of 15 °C for cooling and slow heating at 35 °C, with slow CO_2 exchange. The samples were carefully removed from the CPD machine and mounted on a SEM specimen stub (Ted Pella, USA) with a conductive carbon mount grip on top. The dry samples were placed in a high-resolution sputter coater (Agar Scientific, UK) and coated with 15 nm from gold/palladium filament. All samples imaged on Quanta 200 FEI field emission scanning electron microscopy (Thermo Fisher Scientific, UK).

For histology, after hMSCs were seeded on *ex vivo* explants, the samples were fixed in 10% neutral buffered formalin overnight at room temperature. The tissue pieces were then bathed in 30% sucrose for cryo-sectioning or 70% ethanol. The slices were stained with DAPI as a counterstain to visualize chondrocyte residing cells in the tissue.

4.20. Stem cell adhesion quantification on ex vivo explants

Using a confocal microscope (Leica SP8), six explants with seeded hMSCs were imaged taking six three-dimensional Z-stack images in random allocations. The three-dimensional Z-stack images were flattened to 2D using the Z-project function from the Fiji software package (NIH, USA). Then, a median intensity threshold was applied to the images and the resulting image was changed into binary with a watershed segmentation. Finally, the number of cells were counted excluding sizes smaller than 10 μm.

4.21. Direct membrane functionalisation of cells in bovine cartilage explants

This method was adapted from Krishnan et al. [59]. The 6 mm cartilage bovine *ex vivo* explants were first stained with Hoechst to identify the nuclei of the chondrocyte resident population. Then, the cartilage discs were submerged in a 1 μM solution of either scGFP, scGFP_PlGF2 or [S^-]scGFP_PlGF2 with 1% BSA in 1.5 mL Nalgene tubes for 24 h in a CO_2 atmosphere at 37 °C. The supernatant was collected and submitted to UV–vis analysis taking a spectrum of each solution from 200 to 600 nm. The analysis of the 487 nm absorbance peak was used to quantify the protein deposited on the cartilage. All discs were then fixed in 4% paraformaldehyde (PFA) overnight. A vertical cross section of the discs was cut and analysed using confocal microscopy.

4.22. Statistical analysis

All the data obtained was statistically analysed using a student T-test with two-tailed unpaired samples in Microsoft Excel. Differences between the experimental and control groups were compared. The data was expressed as a mean of at least three biological repeats ±standard deviation. A value of $p < 0.05$ was considered statistically significant and labelled with asterisks (*: $p < 0.05$ and **: $p < 0.01$).

Credit author statement

Rosalia Cuahtecontzi Delint: Methodology, experimental execution, Writing – original draft, data analysis. Graham J. Day: Methodology, experimental execution, data analysis, Writing – review & editing. William. J. P. Macalester: experimental execution, data analysis. Wael Kafienah: Methodology and Supervision. Wenjin Xiao: Supervision, Methodology, experimental execution, Writing – review & editing. Adam W. Perriman: Conceptualization, Supervision, Writing – review & editing.

Data availability

The raw data required to reproduce these findings are available to download from [INSERT PERMANENT WEB LINK(s)]. The processed data required to reproduce these findings are available to download from [INSERT PERMANENT WEB LINK(s)].

Declaration of competing interest

The authors declare that they have no known competing financial interests or personal relationships that could have appeared to influence the work reported in this paper: A.W.P. is the Founder, a Director and a shareholder of CytoSeek, a company engaged in the development of cell membrane reengineering. Work in the Perriman laboratories at the University of Bristol is supported in part by CytoSeek. The remaining authors declare no competing interests.

Acknowledgements

We would like to acknowledge the Wolfson Bioimaging Centre (BBSRC Alert 13 capital grant BB/L014181/1) and Dr Andrew Herman at the Flow Cytometry Facility at the University of Bristol. We also would like to acknowledge the Diamond Light Source (UK) for access to Far-UV SR–CD at beamline B23 and SR–SAXS at beamline B21. We would like to thank Dr D. Frankel for assisting with the microfluidics, Dr Thomas I. P. Green and Dr Robert C. Deller for their support for protein purification techniques, Dr Benjamin Carter for his aid in Fig. 1. We thank the EPSRC (Early Career Fellowship EP/K026720/1), the UKRI (Future Leaders Fellowship MR/S016430/1) for support for Professor Adam. W. Perriman, Consejo Nacional de Ciencia y Tecnologia (CONACyT) and the Bristol Centre for Functional Nanomaterials for support for Rosalia Cuahtecontzi Delint, and Defence science and technology laboratory (Dstl) for funding Graham J. Day. Data are available at the University of Bristol data repository, data.bris, at https://doi.org/10.5523/bris.9r3ofty1lipb2n7x1lnpt3e78.

Appendix A. Supplementary data

Supplementary data to this article can be found online at https://doi.org/10.1016/j.biomaterials.2021.120996.

References

[1] D. Chen, J. Shen, W. Zhao, T. Wang, L. Han, J.L. Hamilton, H.-J. Im, Osteoarthritis: toward a comprehensive understanding of pathological mechanism, Bone Res 5 (2017) 16044.
[2] C.-L. Zhang, T. Huang, B.-L. Wu, W.-X. He, D. Liu, Stem cells in cancer therapy: opportunities and challenges, Oncotarget 8 (2017) 75756–75766.
[3] L. Wei, Z.Z. Wei, M.Q. Jiang, O. Mohamad, S.P. Yu, Stem cell transplantation therapy for multifaceted therapeutic benefits after stroke, Prog. Neurobiol. 157 (2017) 49–78.
[4] A. Leyendecker, C.C.G. Pinheiro, M.T. Amano, D.F. Bueno, The use of human mesenchymal stem cells as therapeutic agents for the in vivo treatment of immune-related diseases: a systematic review, Front. Immunol. 9 (2018) 2056.
[5] J. Freitag, D. Bates, R. Boyd, K. Shah, A. Barnard, L. Huguenin, A. Tenen, Mesenchymal stem cell therapy in the treatment of osteoarthritis: reparative pathways, safety and efficacy - a review, BMC Muscoskel. Disord. 17 (2016) 230.
[6] J.A. McIntyre, I.A. Jones, B. Han, C.T. Vangsness, Intra-articular mesenchymal stem cell therapy for the human joint: a systematic review, Am. J. Sports Med. 46 (2017), 036354651773584.
[7] J. Chahla, N.S. Piuzzi, J.J. Mitchell, C.S. Dean, C. Pascual-Garrido, R.F. LaPrade, G. F. Muschler, Intra-articular cellular therapy for osteoarthritis and focal cartilage defects of the knee: a systematic review of the literature and study quality analysis, J. Bone Joint Surgery Am. 98 (2016) 1511–1521.
[8] M. Yubo, L. Yanyan, L. Li, S. Tao, L. Bo, C. Lin, Clinical efficacy and safety of mesenchymal stem cell transplantation for osteoarthritis treatment: a meta-analysis, PLoS One 12 (2017).
[9] H. Yagi, A. Soto-Gutierrez, B. Parekkadan, Y. Kitagawa, R.G. Tompkins, N. Kobayashi, M.L. Yarmush, Mesenchymal stem cells: mechanisms of immunomodulation and homing, Cell Transplant. 19 (2010) 667–679.
[10] N. Ichiryu, P.J. Fairchild, Immune Privilege of Stem Cells, 2013, pp. 1–16.
[11] G. Chamberlain, J. Fox, B. Ashton, J. Middleton, Concise review: mesenchymal stem cells: their phenotype, differentiation capacity, immunological features, and potential for homing, Stem Cell. 25 (2007) 2739–2749.
[12] Y. Zhang, T. Pizzute, M. Pei, Anti-inflammatory strategies in cartilage repair, Tissue Eng. B Rev. 20 (2014) 655–668.
[13] Y. Zhang, T. Pizzute, M. Pei, Anti-inflammatory strategies in cartilage repair, Tissue Eng. B Rev. 20 (2014) 655–668.
[14] S. Zhang, W.C. Chu, R.C. Lai, S.K. Lim, J.H.P. Hui, W.S. Toh, Exosomes derived from human embryonic mesenchymal stem cells promote osteochondral regeneration, Osteoarthritis Cartilage 24 (2016) 2135–2140.
[15] S. Cosenza, M. Ruiz, K. Toupet, C. Jorgensen, D. Noël, Mesenchymal stem cells derived exosomes and microparticles protect cartilage and bone from degradation in osteoarthritis, Sci. Rep. 7 (2017) 16214.
[16] M.F. Pittenger, A.M. Mackay, S.C. Beck, R.K. Jaiswal, R. Douglas, J.D. Mosca, M. A. Moorman, D.W. Simonetti, S. Craig, D.R. Marshak, Multilineage potential of adult human mesenchymal stem cells, Science 284 (1999) 143–147.
[17] D. Zwolanek, M. Satué, V. Proell, J.R. Godoy, K.I. Odörfer, M. Flicker, S. C. Hoffmann, T. Rülicke, R.G. Erben, Tracking mesenchymal stem cell contributions to regeneration in an immunocompetent cartilage regeneration model, JCI Insight 2 (2017).
[18] P.K. Gupta, A.K. Das, A. Chullikana, A.S. Majumdar, Mesenchymal stem cells for cartilage repair in osteoarthritis, Stem Cell Res. Ther. 3 (2012) 25.
[19] T.D. Henning, R. Gawande, A. Khurana, S. Tavri, L. Mandrussow, D. Golovko, A. Horvai, B. Sennino, D. McDonald, R. Meier, M. Wendland, N. Derugin, T. M. Link, H.E. Daldrup-Link, Magnetic resonance imaging of ferumoxide-labeled mesenchymal stem cells in cartilage defects: in vitro and in vivo investigations, Mol. Imag. 11 (2012) 197–209.
[20] U. Delling, W. Brehm, M. Metzger, E. Ludewig, K. Winter, H. Jülke, In vivo tracking and fate of intra-articularly injected superparamagnetic iron oxide particle-labeled multipotent stromal cells in an ovine model of osteoarthritis, Cell Transplant. 24 (2015) 2379–2390.
[21] M. Satué, C. Schüler, N. Ginner, R.G. Erben, Intra-articularly injected mesenchymal stem cells promote cartilage regeneration, but do not permanently engraft in distant organs, Sci. Rep. 9 (2019) 10153.
[22] X. hong Jing, L. Yang, X. jun Duan, B. Xie, W. Chen, Z. Li, H. bo Tan, In vivo MR imaging tracking of magnetic iron oxide nanoparticle labeled, engineered, autologous bone marrow mesenchymal stem cells following intra-articular injection, Joint Bone Spine 75 (2008) 432–438.
[23] G.D. Jay, K.A. Waller, The biology of Lubricin: near frictionless joint motion, Matrix Biol. 39 (2014) 17–24.
[24] L. Labusca, D.D. Herea, K. Mashayekhi, Stem cells as delivery vehicles for regenerative medicinechallenges and perspectives, World J. Stem Cell. 10 (2018) 43–56.
[25] M.J. Dalby, N. Gadegaard, R.O.C. Oreffo, Harnessing nanotopography and integrin-matrix interactions to influence stem cell fate, Nat. Mater. 13 (2014) 558–569.
[26] E.B. Hunziker, Articular cartilage repair: basic science and clinical progress. A review of the current status and prospects, Osteoarthritis Cartilage 10 (2002) 432–463.
[27] W. Chen, C. Li, M. Peng, B. Xie, L. Zhang, X. Tang, Autologous nasal chondrocytes delivered by injectable hydrogel for in vivo articular cartilage regeneration, Cell Tissue Bank. 19 (2018) 35–46.
[28] P. Smeriglio, J.H. Lai, F. Yang, N. Bhutani, 3D hydrogel scaffolds for articular chondrocyte culture and cartilage generation, JoVE (2015).
[29] J.M. Anderson, A. Rodriguez, D.T. Chang, Foreign body reaction to biomaterials, Semin. Immunol. 20 (2008) 86–100.
[30] I. Gibas, H. Janik, Review: Synthetic polymer hydrogels for biomedical applications, Chem. Chem. Technol. 4 (2010) 297–305.
[31] L. Kock, C.C. Van Donkelaar, K. Ito, Tissue engineering of functional articular cartilage: the current status, Cell Tissue Res. 347 (2012) 613–627.
[32] H. Cheng, M. Byrska-Bishop, C.T. Zhang, C.J. Kastrup, N.S. Hwang, A.K. Tai, W. W. Lee, X. Xu, M. Nahrendorf, R. Langer, D.G. Anderson, Stem cell membrane engineering for cell rolling using peptide conjugation and tuning of cell-selectin interaction kinetics, Biomaterials 33 (2012) 5004–5012.
[33] C.Y. Lo, A. Antonopoulos, A. Dell, S.M. Haslam, T. Lee, S. Neelamegham, The use of surface immobilization of P-selectin glycoprotein ligand-1 on mesenchymal stem cells to facilitate selectin mediated cell tethering and rolling, Biomaterials 34 (2013) 8213–8222.
[34] P.-J. Wu, H. Peng, C. Li, A. Abdel-Latif, B.J. Berron, Adhesive stem cell coatings for enhanced retention in the heart tissue, ACS Appl. Bio Mater. 3 (2020) 2930–2939.
[35] J.P.K. Armstrong, R. Shakur, J.P. Horne, S.C. Dickinson, C.T. Armstrong, K. Lau, J. Kadiwala, R. Lowe, A. Seddon, S. Mann, J.L.R. Anderson, A.W. Perriman, A. P. Hollander, Artificial membrane-binding proteins stimulate oxygenation of stem cells during engineering of large cartilage tissue, Nat. Commun. 6 (2015) 7405.
[36] R.C. Deller, T. Richardson, R. Richardson, L. Bevan, I. Zampetakis, F. Scarpa, A. W. Perriman, Artificial cell membrane binding thrombin constructs drive in situ fibrin hydrogel formation, Nat. Commun. 10 (2019) 1887.
[37] W. Xiao, T.I.P. Green, X. Liang, R.C. Delint, G. Perry, M.S. Roberts, K. Le Vay, C. R. Back, R. Ascione, H. Wang, P.R. Race, A.W. Perriman, Designer artificial membrane binding proteins to direct stem cells to the myocardium, Chem. Sci. (2019).
[38] M.M. Martino, P.S. Briquez, E. Guc, F. Tortelli, W.W. Kilarski, S. Metzger, J.J. Rice, G.A. Kuhn, R. Muller, M.A. Swartz, J.A. Hubbell, Growth factors engineered for super-affinity to the extracellular matrix enhance tissue healing, Science 343 (2014) 885–888.
[39] M.S. Lawrence, K.J. Phillips, D.R. Liu, Supercharging proteins can impart unusual resilience, J. Am. Chem. Soc. 129 (2007) 10110–10112.
[40] A. Roy, A. Kucukural, Y. Zhang, I-TASSER: a unified platform for automated protein structure and function prediction, Nat. Protoc. 5 (2010) 725–738.
[41] J.D. Pédelacq, S. Cabantous, T. Tran, T.C. Terwilliger, G.S. Waldo, Engineering and characterization of a superfolder green fluorescent protein, Nat. Biotechnol. 24 (2006) 79–88.
[42] B. Hammouda, A new Guinier-Porod model, J. Appl. Crystallogr. 43 (2010) 716–719.
[43] A.W. Perriman, A.P.S. Brogan, H. Cölfen, N. Tsoureas, G.R. Owen, S. Mann, Reversible dioxygen binding in solvent-free liquid myoglobin, Nat. Chem. 2 (2010) 622–626.
[44] A.P.S. Brogan, R.B. Sessions, A.W. Perriman, S. Mann, Molecular dynamics simulations reveal a dielectric-responsive coronal structure in protein-polymer surfactant hybrid nanoconstructs, J. Am. Chem. Soc. 136 (2014) 16824–16831.
[45] J.J. Cronican, D.B. Thompson, K.T. Beier, B.R. McNaughton, C.L. Cepko, D.R. Liu, Potent delivery of functional proteins into Mammalian cells in vitro and in vivo using a supercharged protein, ACS Chem. Biol. 5 (2010) 747–752.
[46] B.R. McNaughton, J.J. Cronican, D.B. Thompson, D.R. Liu, Mammalian cell penetration, siRNA transfection, and DNA transfection by supercharged proteins, Proc. Natl. Acad. Sci. Unit. States Am. 106 (2009) 6111–6116.
[47] D.B. Thompson, R. Villaseñor, B.M. Dorr, M. Zerial, D.R. Liu, Cellular uptake mechanisms and endosomal trafficking of supercharged proteins, Chem. Biol. 19 (2012) 831–843.
[48] T. Farrugia, A.W. Perriman, K.P. Sharma, S. Mann, Multi-enzyme cascade reactions using protein-polymer surfactant self-standing films, Chem. Commun. 53 (2017) 2094–2097.
[49] K.P. Sharma, A.M. Collins, A.W. Perriman, S. Mann, Enzymatically active self-standing protein-polymer surfactant films prepared by hierarchical self-assembly, Adv. Mater. 25 (2013) 2005–2010.
[50] K.P. Sharma, R. Harniman, T. Farrugia, W.H. Briscoe, A.W. Perriman, S. Mann, Dynamic behavior in enzyme-polymer surfactant hydrogel films, Adv. Mater. 28 (2016) 1597–1602.
[51] J. Shang, H. Liu, J. Li, Y. Zhou, Roles of hypoxia during the chondrogenic differentiation of mesenchymal stem cells, Curr. Stem Cell Res. Ther. 9 (2014) 141–147.
[52] K.S. Cheah, N.G. Stoker, J.R. Griffin, F.G. Grosveld, E. Solomon, Identification and characterization of the human type II collagen gene (COL2A1), Proc. Natl. Acad. Sci. U. S. A 82 (1985) 2555–2559.
[53] M. Migdal, B. Huppertz, S. Tessler, A. Comforti, M. Shibuya, R. Reich, H. Baumann, G. Neufeld, Neuropilin-1 is a placenta growth factor-2 receptor, J. Biol. Chem. 273 (1998) 22272–22278.
[54] R.K. Okolicsanyi, E.T. Camilleri, L.E. Oikari, C. Yu, S.M. Cool, A.J. Van Wijnen, L. R. Griffiths, L.M. Haupt, Human mesenchymal stem cells retain multilineage differentiation capacity including neural marker expression after extended in vitro expansion, PLoS One 10 (2015).
[55] R. Nalim, K. Pekkan, H. Bin Sun, H. Yokota, Oscillating Couette flow for in vitro cell loading, J. Biomech. 37 (2004) 939–942.

[56] K. Pekkan, R. Nalim, H. Yokota, Computed synovial fluid flow in a simple knee joint model, in: Proceedings of the 4th ASME/JSME Joint Fluids Engineering Conference, 2003, pp. 1–5.
[57] H. Bin Sun, R. Nalim, H. Yokota, Expression and activities of matrix metalloproteinases under oscillatory shear in IL-1-stimulated synovial cells, Connect. Tissue Res. 44 (2003) 42–49.
[58] G. Monaco, A.J. El Haj, M. Alini, M.J. Stoddart, Ex vivo systems to study chondrogenic differentiation and cartilage integration, JFMK 6 (2021) 6.
[59] Y. Krishnan, H.A. Rees, C.P. Rossitto, S.-E. Kim, H.-H.K. Hung, E.H. Frank, B. D. Olsen, D.R. Liu, P.T. Hammond, A.J. Grodzinsky, Green fluorescent proteins engineered for cartilage-targeted drug delivery: insights for transport into highly charged avascular tissues, Biomaterials 183 (2018) 218–233.
[60] J. Ishihara, L. Potin, H.M. Larsson, P. Hosseinchi, M.A. Swartz, A. Ishihara, G. Galliverti, J.A. Hubbell, K. Fukunaga, Matrix-binding checkpoint immunotherapies enhance antitumor efficacy and reduce adverse events, Sci. Transl. Med. 9 (2017), eaan0401.
[61] D.K.W. Ocansey, B. Pei, Y. Yan, H. Qian, X. Zhang, W. Xu, F. Mao, Improved therapeutics of modified mesenchymal stem cells: an update, J. Transl. Med. 18 (2020) 42.
[62] A.D. Becker, I.V. Riet, Homing and migration of mesenchymal stromal cells: how to improve the efficacy of cell therapy? World J. Stem Cell. 8 (2016) 73.
[63] A. Micsonai, F. Wien, L. Kernya, Y.H. Lee, Y. Goto, M. Refregiers, J. Kardos, Accurate secondary structure prediction and fold recognition for circular dichroism spectroscopy, Proc. Natl. Acad. Sci. Unit. States Am. 112 (2015) E3095–E3103.
[64] F.E. Reyes, C.R. Schwartz, J.A. Tainer, R.P. Rambo, Methods for using new conceptual tools and parameters to assess RNA structure by small-angle X-ray scattering, Methods Enzymol. 549 (2014) 235–263.
[65] S. Skou, R.E. Gillilan, N. Ando, Synchrotron-based small-angle X-ray scattering of proteins in solution, Nat. Protoc. 9 (2014) 1727–1739.
[66] D. Franke, D.I. Svergun, DAMMIF, a program for rapid ab-initio shape determination in small-angle scattering, J. Appl. Crystallogr. 42 (2009) 342–346.